Development of the Gas Puff Charge Exchange Recombination Spectroscopy (GP-CXRS) Technique for Ion Measurements in the Plasma Edge

R.M. Churchill,[1, a)] C. Theiler,[1] B. Lipschultz,[1] T. Pütterich,[2] E. Viezzer,[2] and the Alcator C-Mod and ASDEX Upgrade Teams

[1)] *MIT Plasma Science and Fusion Center, Cambridge, USA*

[2)] *Max-Planck-Institut für Plasmaphysik, EURATOM Association, Boltzmannstraße 2, D-85748 Garching, Germany*

(Dated: 30 July 2013)

A novel charge-exchange recombination spectroscopy (CXRS) diagnostic method is presented, which uses a simple thermal gas puff for its donor neutral source, instead of the typical high-energy neutral beam. This diagnostic, named gas puff CXRS (GP-CXRS), is used to measure ion density, velocity, and temperature in the tokamak edge/pedestal region with excellent signal-background ratios, and has a number of advantages to conventional beam-based CXRS systems. Here we develop the physics basis for GP-CXRS, including the neutral transport, the charge-exchange process at low energies, and effects of energy-dependent rate coefficients on the measurements. The GP-CXRS hardware setup is described on two separate tokamaks, Alcator C-Mod and ASDEX Upgrade. Measured spectra and profiles are also presented. Profile comparisons of GP-CXRS and a beam based CXRS system show good agreement. Emphasis is given throughout to describing guiding principles for users interested in applying the GP-CXRS diagnostic technique.

I. INTRODUCTION

Charge eXchange Recombination Spectroscopy (CXRS, also known as CHERS, CERS, or CXS) is a well-known, mature plasma diagnostic technique used to derive information about ion species in a plasma, such as ion density, ion temperature, and ion bulk velocity[1,2]. The basic idea behind CXRS is to inject neutral atoms (D^0) into the plasma, which will then undergo charge-exchange (CX) reactions with plasma ions (A^{Z+}):

$$A^{Z+} + D^0 \rightarrow A^{(Z-1)+*} + D^{1+} \qquad (1)$$
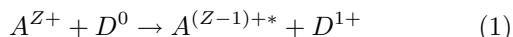
The newly formed excited atoms $(A^{(Z-1+)*})$ radiatively decay, emitting photons which are then collected by optics. Injecting neutrals into the plasma allows localization of the CX reactions to the intersection of the optics line-of-sight and the injected neutrals path. Most CXRS diagnostic systems utilize a high energy (50-100keV range) neutral beam to localize CX reactions. Here we present a novel, alternative CXRS system which uses a simple thermal gas puff to inject neutrals into the plasma.

This alternate system, which we will refer to as GP-CXRS (gas puff CXRS), offers many advantages over a conventional CXRS system which uses high energy neutral beams. First, the apparatus to inject room-temperature gas is simple, inexpensive, and easy to maintain, whereas high energy neutral beams are large devices which are expensive both in terms of initial cost and maintenance. Second, gas delivery tubes can be placed almost anywhere around the plasma containment vessel, allowing ion measurements at plasma locations not normally accessible to high energy neutral beams, such as the inboard (high-field side or HFS) of a tokamak. This opens up studies of previously inaccessible physics, such as variations in impurity ion density and velocity on a flux-surface[3–5]. Third, the emission region is narrower, since the gas puff produces a neutral cloud that is smaller in width than a typical high energy neutral beam. This helps avoid smearing effects on the profile measurements[1]. Fourth, compared to some high-energy beam-based CXRS systems, the signal-background ratio is much larger in the GP-CXRS system (typically 10x or more, dependent on beam current and size) in the edge/pedestal region, due mainly to the increased neutral density. This can be especially beneficial in the steep gradient regions of the pedestal[6].

The main disadvantage of the GP-CXRS system compared to a high-energy beam CXRS system is the rapid decay of signal further into the core of the plasma, due to the decreased penetration depth of the slow neutrals produced by the gas puff. In tokamaks, the GP-CXRS system is therefore effectively limited to making measurements in the edge region $(r/a > 0.85)$. However, this covers the pedestal region, which is critical to the overall performance of tokamak plasmas through profile stiffness[7] and turbulence reduction by sheared $E \times B$ flow[8]. CXRS diagnostics are one of the principle diagnostics for measuring the radial electric fiedl (E_r) used in calculating the $E \times B$ flow. Extending the predictive capabilities and physics understanding of the pedestal region is an active area of research[9].

Several machines have used results from GP-CXRS systems in published physics papers, among them Alcator C-Mod[3], ASDEX Upgrade[4], and MAST[10], though none have described the diagnostic technique in detail. The focus of this paper will be to provide the physics basis for the GP-CXRS system, including related diagnostic issues, to guide users interested in applying the technique.
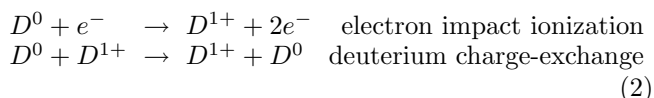
a) Electronic mail: rmchurch@mit.edu

The GP-CXRS system installed on the Alcator C-Mod tokamak[11] will be used as the primary example to discuss implementation details. The outline of the paper is as follows: Section II discusses the transport of the gas puff neutrals into the plasma. Section III reviews charge-exchange at low energy, and shows how to calculate the effective thermal-thermal CX rate coefficient. In Section IV we calculate the effect of energy-dependent rate coefficients on the plasma parameters derived from GP-CXRS parameters. Section V discusses details for estimating the signal from a given flow rate of gas puff particles. In Section VI, we describe the implementation of GP-CXRS on Alcator C-Mod. In Section VII we present GP-CXRS spectra and derived plasma profiles, and discuss special topics in the analysis of GP-CXRS spectra. In Section VIII the GP-CXRS system on ASDEX Upgrade is reviewed, and profiles are presented. Finally, in Section IX we benchmark the GP-CXRS profiles against those from a high energy beam CXRS system.

II. TRANSPORT OF NEUTRALS PRODUCED BY A GAS PUFF

The transport into the plasma of neutrals produced from a gas puff is different from that of neutrals produced by a high-energy beam, mainly due to differences in the energy distribution. The gas puff neutrals have a thermal distribution of energies, which approaches the plasma temperature ($E \sim T_i$). This is in contrast to high-energy beam neutrals, which have fairly discrete energies that are typically much larger than the plasma temperature ($E \gg T_i$). In this section we will develop a picture of the transport of the gas puff neutrals, and show simulation results of the shape and particle density of the gas puff neutral cloud, which is important for GP-CXRS. In the following discussion, we will assume the gas species used is molecular deuterium (D_2), although in practice other gas types can be used with varying benefits (see Section VII B on spectral contamination by molecular lines).

A simple picture of the production of a neutral from a gas puff and its subsequent transport into the plasma is as follows: a room temperature D_2 gas molecule travels into the edge of the plasma, where it quickly undergoes Franck-Condon dissociation into two separate deuterium (D) neutral atoms, each with kinetic energy of $\sim$3 eV. These neutrals dissociate isotropically, so generally one neutral will continue further into the plasma, and the other will return towards the wall. The neutrals continuing into the plasma will penetrate until being ionized by electron-impact, or charge-exchanging with a background plasma deuterium ion:

$$
\begin{aligned}
D^0 + e^- &\rightarrow D^{1+} + 2e^- \quad \text{electron impact ionization} \\
D^0 + D^{1+} &\rightarrow D^{1+} + D^0 \quad \text{deuterium charge-exchange}
\end{aligned}
$$
$$(2)$$

Even in the scrape-off layer (SOL), a region of low temperature and density, these Franck-Condon neutrals have a mean-free path on the order of the distance to the separatrix[12], clearly an undesirable situation given that we need a significant population of neutrals penetrating beyond the pedestal region. However, the charge-exchange process produces additional generations of neutrals which can then penetrate further into the plasma[13]. These neutrals produced by charge-exchange retain the energy of the background plasma ions from which they came, so that with sufficient charge-exchange reactions, the neutral population takes on an energy distribution approaching that of the background plasma ion distribution.

To give quantitative results of the neutral penetration, fluid approximations could be used, as is often done in neutral transport problems. Neutrals are treated as either diffusive[14], which leads to a neutral penetration depth of $\delta \sim (\lambda_{ion}\lambda_{cx})^{\frac{1}{2}} \sim \frac{v_{th}}{n_e(\langle\sigma v\rangle_{ion}\cdot\langle\sigma v\rangle_{cx})^{\frac{1}{2}}}$, or free-streaming[15], leading to a neutral penetration depth of $\delta \sim \lambda_{ion} \sim \frac{V_n}{n_e\langle\sigma v\rangle_{ion}}$. The diffusive nature makes sense when charge-exchange reactions dominate over ionization, as the CX reactions act as a randomizing event, leading to a random walk problem with a step size of λ_{cx}. The free-streaming would be more appropriate if the ionization rate were much larger than the CX rate.

Unfortunately these fluid approximations are too simple for most cases involving neutral transport in the edge/pedestal region. To properly give a more detailed, quantitative treatment of the production and transport of the gas puff neutrals requires the use of numerical, kinetic neutral transport codes. The reasons requiring a kinetic treatment over the simpler fluid treatments are (1) the gradient scale lengths in the pedestal region are often smaller than the neutral mean-free path, violating the fluid approximation and (2) the CX and ionization rate coefficients, $\langle\sigma v\rangle$, are of the same order for a significant temperature range[16], as seen in Fig. 1. This range of temperatures basically covers the range of temperatures seen in the pedestal region in most current tokamak devices.

Several kinetic codes exist to simulate neutral transport, the most popular being full 3D Monte Carlo codes such as DEGAS2[18] and EIRENE[19], which are often coupled to 2D fluid codes such as UEDGE, OSM, and B2, to provide full simulation of neutral transport in a background plasma. These codes can offer a complete picture of the gas puff neutral transport at the expense of long code execution times, in order to have good statistics. A simpler code that treats the neutral transport problem analytically is KN1D[20], though it uses a simplified 1D slab geometry.

To study the shape and particle density of the gas puff neutral cloud, OSM-EIRENE simulations were undertaken for a number of different plasma conditions, ranging from L-mode plasmas with low T_e and n_e to H-mode and I-mode plasmas with large gradients in the pedestal region. The results are shown in Fig. 2 for simulations with gas injected from the outer-wall, with
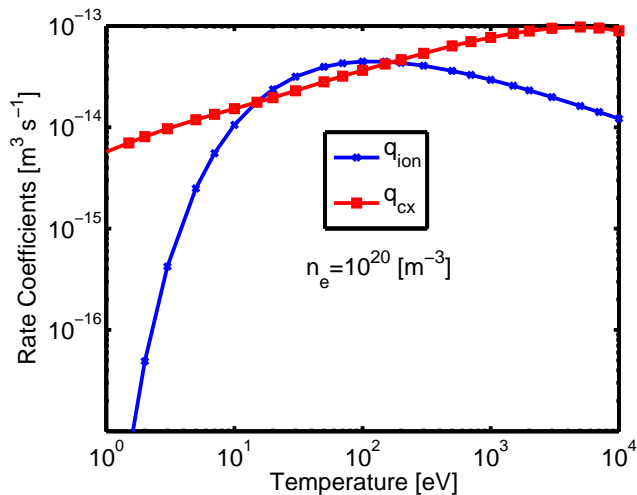
FIG. 1. Electron-impact ionization and deuterium-deuterium charge-exchange rate coefficients. Taken from ADAS adf11 files[17]

Fig. 2(a) showing the neutral density along the center-line of the gas puff, $n_{D0}(R)$, where R is the major radius, and Fig.2(b) showing the $1/e$ point of the neutral density, $n_D(R, \eta)$, from the gas puff center-line value, in the transverse direction η. As seen, despite the wide range of plasma parameters, the resulting gas puff shape is very similar for all simulations, and can be described by the following diverging Gaussian beam-like formula:

$$n_D(R, \eta) = n_{D0}(R) e^{-\left(\frac{\eta}{W(R)}\right)^2} \qquad (3)$$

where W(R) describes the diverging width of the Gaussian beam:

$$W(R) = w_0 \left(1 + \frac{|R - R_{puff}|}{w_0} tan(\theta_0)\right) \qquad (3b)$$

where R_{puff} is the major radius where the gas exits the delivery tube and enters the vacuum chamber, w_0 represents what the beam width *would* be (not actually *is*) at R_{puff} if the gas puff was a pure truncated cone, and θ_0 is the divergence half-angle of the gas puff (see Fig. 2(b) for a picture of these parameters). Note that this doesn't necessarily describe the gas puff cloud outside of the separatrix, as the simulation grid was sparse outside of the separatrix. For a gas puff at the outer-midplane, with $R_{puff} - R_{separatrix} \sim 2$ cm, and assuming a cosine distribution of gas molecules entering the plasma, the parameters were fit to be $w_0 \approx 1.1$ cm, and $\theta_0 \approx 23°$. Note also from Fig.2 that while a single angle θ_0 parameter describes all of the simulations, the $n_{D0}(R)$ profile varied over several orders of magnitude. No simple scaling was found for the $n_{D0}(R)$ profile shape with n_e or T_e, nor was the $n_{D0}(R)$ profile shape adequately explained by simple neutral penetration models, like $sech^2(\frac{|R-R_{puff}|}{\sqrt{\lambda_{cx}\lambda_{ion}}})$ or $exp(-\frac{\langle\sigma_{ion}v\rangle}{V_n}\int n_e dR)$, showing the importance of treating the neutral transport problem kinetically.
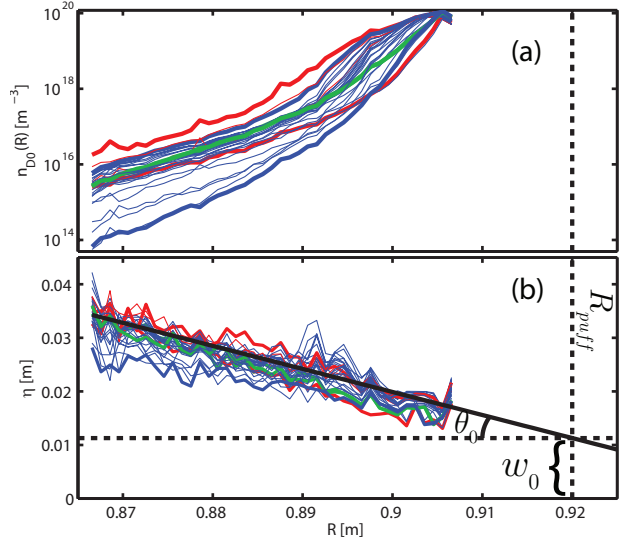

FIG. 2. OSM-EIRENE simulation results over a wide range of input n_e and T_e profiles: H-modes (blue), I-modes (red), and L-modes (green). Bold lines show the high and low n_{D0} from each group. In (a) is shown the center-line D^0 density from the puff, $n_{D0}(R)$ and in (b) the $1/e$ point in the transverse direction of n_D from the center line value n_{D0}, showing the puff shape stays the same over a wide range of parameters.

These simulations also resolve the velocity distribution of the neutrals, allowing calculation of the neutral temperature, $T_D = \frac{2}{3}\langle E \rangle$. T_D is consistently lower than the background plasma temperature, as shown in Fig. 3. This is expected, as the charge-exchanged neutrals can travel to regions of temperature different from that of their local birth location[21]. Other numerical simulations have shown this as well[22]. This difference will introduce an error in the CX rate coefficient if not accounted for, as will be shown in Section III.

While relying solely on simulations to deduce the gas puff densities requires further validation studies, these simulation results show two important features of the transport of the gas puff neutrals: (1) the neutral cloud resulting from the gas puff has a small-angle spread and (2) the neutral temperature, T_D, is consistently lower, but approaches the background plasma temperature T_e. From multiple simulations, the ratio of T_D/T_e inside the separatrix and towards the core is usually in a range of $0.3 < T_D/T_e < 0.8$. This range of T_D/T_e holds true for simulations using parameters from either Alcator C-Mod, or ASDEX Upgrade.

III. CHARGE EXCHANGE OF IMPURITIES WITH NEUTRALS FROM A GAS PUFF

The charge-exchange process is also affected by the lower energy and thermal distribution of the gas puff neu-
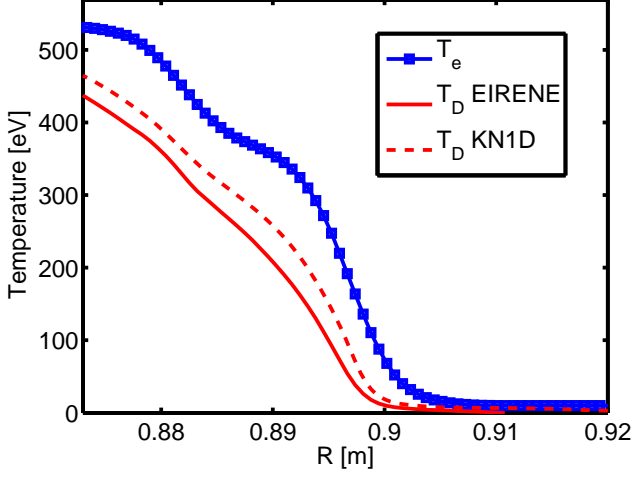
FIG. 3. Simulated neutral temperature (T_D, in red) vs input measured electron temperature (T_e, in blue), showing the neutral temperature is generally lower than the electron temperature.

FIG. 4. Partial cross-sections for electron-capture into the n' excited state of B^{5+} with D^0. Solid lines (___) are for collision energies of 0.25 keV/amu, dotted lines(- - -) are for 50 keV/amu. The $n^D = 3$ cross-sections at low energy are not available[26], and so were scaled from the $n^D = 2$ cross-sections.

trals. This is due to a number of peculiarities of the CX process which will be reviewed and discussed here in the context of GP-CXRS. As will be shown, depending on the impurity species and the transition used, excited states of the neutral can have a much larger, even dominant, contribution to the CXRS signal.

Charge-exchange is a resonant process, and as a result the donor electron will preferentially populate excited states of the receiver ion that conserve the electron's orbital energy and radius[23]. The prefered, resonant excited state of the impurity ion is:

$$n'_{res} = n^D \left(\frac{Z'}{Z^D} \right)^{\frac{3}{4}} \qquad (4)$$

where n^D and Z^D are the principal quantum number and nuclear charge of the donor species (the D neutral atom), and n' and Z' are the principal quantum number and charge of the receiver species (the impurity A^{Z+}). This equation is valid for a large range of interacting energies[23,24]. At low collision velocities, the resonant character is pronounced, leading to large partial CX cross-sections $\sigma_{cx}(n')$ only at or near the excited state n'_{res}. As the interaction energy increases to intermediate energy levels typical of neutral beams, different mechanisms start contributing to the resonant reactions, leading to a broadened n'-distribution of the partial CX cross-sections, as shown in Fig. 4. Additionally, in the low collision energy regime the total CX cross-section scales like $\sigma_{cx,tot,lowE} \propto (n^D)^4$, while the intermediate collision energy regime scales oppositely[25], $\sigma_{cx,tot,intE} \propto \frac{1}{(n^D)^3}$.

These three charge-exchange attributes at low collision energy (preferential excited state n'_{res} of receiver, narrow n'-distribution of partial CX cross-section, and increasing total CX cross-section with n^D) lead
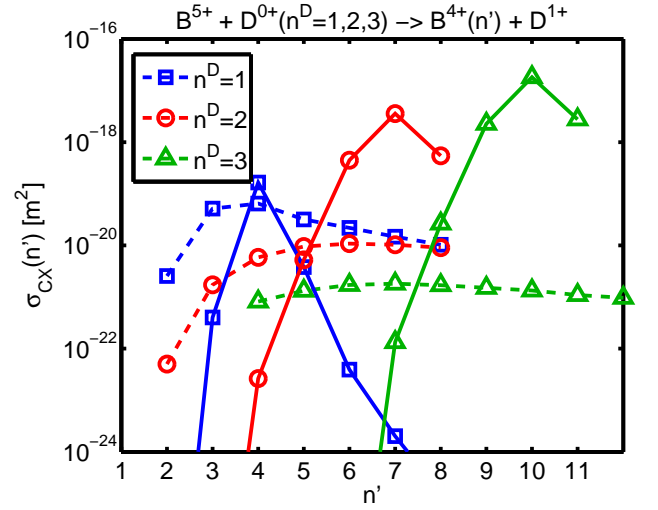
to the excited neutrals playing a much more significant photon generating role in GP-CXRS than in high-energy beam CXRS. Figure 4 illustrates this point and shows all three CX attributes, for a low energy (0.25keV/amu, solid lines) and an intermediate energy (50keV/amu, dotted lines), using as an example the $B^{5+} + D^0(n^D = 1, 2, 3) \rightarrow B^{4+}(n') + D^{1+}$ reaction. For the diagnostically relevant $n' = 7$ reaction (used for the Alcator C-Mod GP-CXRS system), the $D(n^D = 2)$ cross-section is over 4 orders of magnitude larger than the $D(n^D = 3)$ cross-section, and over 6 orders of magnitude larger than the $D(n^D = 1)$. Despite the small fraction of excited neutrals (typically $\frac{n_D(n^D=2)}{n_D(n^D=1)} \sim 1\%$), they will often make the dominant contribution to the GP-CXRS signal. It should be noted that $A^{Z+} + D(n^D = 2)$ being the dominant reaction is a general result for most common applications of GP-CXRS. This is due to a combination of the facts that pedestal CXRS systems typically use low-Z impurities ($Z \leq 10$) with low ionization energies, which guarantee a large population of fully-ionized impurities in the pedestal, and atomic transitions that emit photons in the visible region (400nm-700nm), as the optics are simpler.

Of course, the above are simply guidelines; for quantitative results, such as for accurate ion density measurements or GP-CXRS signal estimation, the effective CX rate coefficients must be calculated. In its general form, the rate coefficient for CX into a particular level n' is calculated integrating over the distributions of the interacting ion and the neutral:

$$\langle \sigma_{cx}(n')v \rangle = \frac{\iint d\mathbf{v}_D d\mathbf{v}_Z \, \sigma_{cx}(n', |\mathbf{v}_D - \mathbf{v}_Z|) |\mathbf{v}_D - \mathbf{v}_Z| f_D(\mathbf{v}_D) f_Z(\mathbf{v}_Z)}{\iint d\mathbf{v}_D d\mathbf{v}_Z \, f_D(\mathbf{v}_D) f_Z(\mathbf{v}_Z)}$$

$$(5)$$

For neutral beam systems, the beam velocity distributions are mono-energetic, i.e. discrete delta-functions, $f_D(\mathbf{v}_D) = n_D\delta(\mathbf{v}_D - \mathbf{u}_{beam})$, and Eq. (5) reduces to a 1D integral if the impurity ion species is Maxwellian. For GP-CXRS, the thermal distribution of the neutrals requires averaging over both species velocity distributions. If we assume both the impurity ions and the neutrals have Maxwellian velocity distributions, while allowing them to have different temperatures, Eq. (5) reduces to:

$$\langle\sigma_{cx}v\rangle = \sqrt{\frac{8}{\pi m_r}}\frac{1}{T_{eff}^{\frac{3}{2}}}\int_0^\infty dE\,\sigma_{cx}(E)Ee^{-\frac{E}{T_{eff}}} \qquad (6)$$

where

m_r Reduced mass, $\frac{m_Z m_D}{m_Z + m_D}$ [kg]

T_{eff} Effective temperature, $\frac{m_D T_Z + m_Z T_D}{m_D + m_Z}$ [J]

E Center-of-mass energy, $\frac{1}{2}m_r|\mathbf{v}_Z - \mathbf{v}_D|^2$

Here bulk-velocity has been neglected in both species, since it was found that large differences between the bulk velocity of the neutrals and that of the impurity ions of > 60 km/s were needed to make a 10% difference in $\langle\sigma_{cx}v\rangle$. The thermal-thermal averaged rate coefficient in Eq. (6), which uses different temperatures ($T_Z \neq T_D$), has the same form of the thermal-thermal rate coefficient using equal temperatures[27], ($T_Z = T_D$), except that the equal temperature is replaced by the effective temperature, T_{eff}. Using this thermal-thermal rate coefficient, the effective CX rate coefficient, $q_{eff}(n' \to n'')$, is then formed by taking into account the branching ratio of the specific atomic transition, $n' \to n''$, cascades from states above n', and l-mixing of the states[1]. The effective thermal-thermal CX rate coefficient can be calculated using a combination of the ADAS314 and ADAS308 codes, creating a lookup table of q_{eff} values depending on the plasma parameters of n_e, T_e, and Z_{eff}. While these codes only treat same temperature receiver and donor, the effective temperature T_{eff} (see Eq. (6)) can be used for the temperature in the lookup tables of q_{eff} for the case of unequal temperatures.

As shown from neutral transport simulations in Section II, the neutral temperature can be different from the background plasma temperature. In principle, measurements of the temperature of the gas puff neutrals can be made spectroscopically[28]. However, if the neutral temperature is unknown or uncertain, the relative error in the CX rate coefficient can be calculated by using a value in the middle of the expected range, i.e $T_D = 0.5T_Z$. Since the CX cross-section of interest for GP-CXRS systems are relatively flat at low energies, a simple analytical upper bound on the relative error can be found. Taking σ_{cx} to be constant reduces Eq. (6) to $\langle\sigma_{cx}v\rangle \approx \sigma_{cx}v_{th}$, producing a relative error, $\epsilon_{\langle\sigma v\rangle}$:

$$\begin{aligned}\epsilon_{\langle\sigma v\rangle} &= \frac{\left|\sqrt{T_{eff}|_{T_D=0.5T_Z}} - \sqrt{T_{eff}}\right|}{\sqrt{T_{eff}}} \\ &= \left|1 - \sqrt{\frac{m_D + 0.5m_Z}{m_D + m_Z \cdot \frac{T_D}{T_Z}}}\right|\end{aligned} \qquad (7)$$

This upper-bound on the relative error (Eq.(7)) is shown in green on Figure 5, along with relative errors using the actual CX cross-section in the integral of Eq.(6). Of course, neutral simulations can be used to determine the neutral temperature, T_D, and reduce this error $\epsilon_{\langle\sigma v\rangle}$ considerably, but this upper bound error shows that, in the expected T_D/T_Z range, the maximum relative error of $\langle\sigma v\rangle$ assuming $T_D = 0.5T_Z$ is less than 20%.
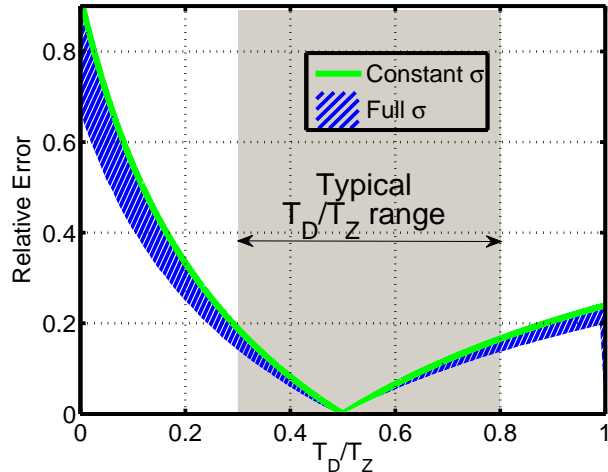

FIG. 5. Error made in the thermal-thermal CX rate coefficient when assuming a scaled neutral temperature of $T_D = 0.5T_Z$. Typical range of T_D/T_Z from simulation is 0.3 to 0.8

An example of the ADAS calculated thermal-thermal effective CX rate coefficient, q_{eff}, appropriate for use with GP-CXRS is shown in Fig. 6, for the $B^{5+} + D(n^D = 1, 2) \to B^{4+}(n' = 7) + D^{1+} \to B^{4+}(n'' = 6) + D^{1+} + h\nu$ reaction. Also shown is q_{eff} multiplied by the excited state fraction, which shows the relative amount of CXRS signal photons each neutral fraction is producing. Excited state fractions were determined by the ADAS photon emissivity coefficients (PEC)[17]:

$$\frac{n_D(n^D = 2)}{n_D(n^D = 1)} = \frac{PEC_{21}^{EXC}}{A_{21}}n_e \qquad (8)$$

where A_{21} is the Einstein coefficient for the $n^D = 2 \to 1$ transition, and PEC_{21}^{EXC} are the ADAS photon emissivity coefficients (PEC). Here and elsewhere in this paper, the recombination PEC is neglected, as it is negligible at temperatures above a few eV. The charge-exchange PEC is also neglected, as the deuterium-deuterium charge-exchange process will dominantly produce products that are the same as reactants, giving no net change in excited state populations. As seen in Fig. 6(b), for densities larger than $n_e \sim 10^{19}[m^{-3}]$, the $D(n^D = 2)$ excited state fraction will make the dominant contribution to the total emitted CXRS light.
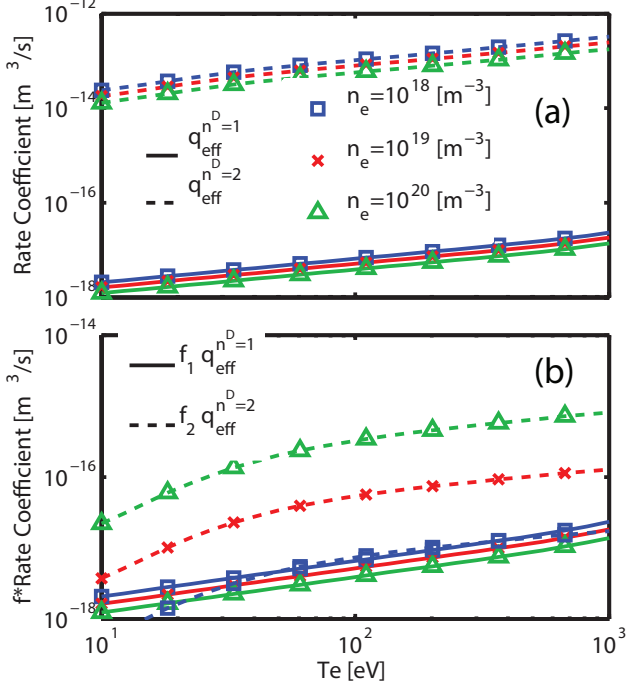
FIG. 6. (a) $BV(7 \to 6)$ effective CX rate coefficient, $q_{eff}^{n^D=1,2}$ and (b) $q_{eff}^{n^D=1,2}$ multiplied by the neutral density excited state fraction, $f_i = n_D(n^D = i)/n_D(n^D = 1)$. This represents the amount of light each excited neutral species contributes to the total CX signal.

IV. ENERGY DEPENDENT RATE-COEFFICIENT EFFECTS

Energy dependent rate coefficients can also have an influence on the apparent temperature and flow of the impurity ions. For CXRS with a high-energy neutral beam, such energy dependent cross-section effects have been investigated extensively[29–31]. Here, we treat this problem for GP-CXRS, where the situation is qualitatively different in the sense that the velocity of the donor particles is of the same order as that of the impurity ions.

To quantitatively evaluate measurement errors associated with energy dependent rate coefficients, we need the general expression for the emitted number of photons per unit of time, volume, and wavelength induced by charge exchange (CX) reactions between the donor particles D and the receiver particles A^{Z+} (the impurity ions). We indicate this quantity, the spectral emissivity, with ε^λ, such that

$$\varepsilon^\lambda \mathrm{d}\lambda = \left[\iint \mathrm{d}\mathbf{v}_D \cdot \mathrm{d}\mathbf{v}_{\perp Z} \cdot f_D(\mathbf{v}_D) \cdot f_Z(\mathbf{v}_Z) \cdot \right.$$
$$\left. |\mathbf{v}_Z - \mathbf{v}_D| \cdot \sigma_{cx,eff}(|\mathbf{v}_Z - \mathbf{v}_D|) \right] \cdot \mathrm{d}v_{\|Z}. \quad (9)$$

Here, $\mathbf{v}_D$ ($\mathbf{v}_Z$) and f_D (f_Z) are the velocity and velocity distribution function of the donor (receiver) particles, $\perp$ and $\|$ indicate the velocity components w.r.t. the line of sight, and $\sigma_{cx,eff}$ is the effective emission charge exchange cross section for the transition of interest, in our case $n = 7 \to 6$ of B^{4+}. The integral is five dimensional and performed over $\mathbf{v}_D$ and $\mathbf{v}_{\perp Z}$. For non-relativistic velocities of the impurity ions, the emitted wavelength λ and $\mathrm{d}\lambda$ are linked to $v_{\|Z}$ and $\mathrm{d}v_{\|Z}$ by

$$\lambda - \lambda_0 = \frac{\lambda_0}{c} \cdot v_{\|Z}, \quad \mathrm{d}\lambda = \frac{\lambda_0}{c} \mathrm{d}v_{\|Z}, \quad (10)$$

with λ_0 the rest wavelength of the transition and c the speed of light.

Before solving Eqs. (9) and (10) for realistic cases, we first consider a simplified situation for illustration. We assume that the neutrals in the gas puff are cold and have zero drift, thus $\mathbf{v}_D = 0$. We further assume Maxwellian impurity ions with an arbitrary drift $\mathbf{u}_Z = \langle \mathbf{v}_Z \rangle$ (here, brackets indicate an average over the velocity distribution function). Eqs. (9) and (10) then simplify to

$$\varepsilon^\lambda \propto \int \mathrm{d}\mathbf{v}_{\perp Z} \cdot f_{\perp Z}^M(\mathbf{v}_{\perp Z} - \mathbf{u}_{\perp Z}) \cdot |\mathbf{v}_Z| \cdot \sigma_{cx,eff}(|\mathbf{v}_Z|)$$
$$\cdot \exp\left(\frac{-(\lambda - \lambda_1)^2}{2 \left(\sqrt{\frac{T_Z}{m_Z}} \frac{\lambda_0}{c} \right)^2} \right) \quad (11)$$

where $f_{\perp Z}^M$ is a two-dimensional Maxwellian with temperature T_Z and mass m_Z, and we have defined λ_1 as

$$\lambda_1 = \lambda_0 \cdot (1 + u_{\|Z}/c). \quad (12)$$

The variable $|\mathbf{v}_Z|$ is expressed as a function of $\mathbf{v}_{\perp Z}$ and λ:

$$|\mathbf{v}_Z| = \sqrt{\mathbf{v}_{\perp Z}^2 + \left(\frac{c}{\lambda_0}(\lambda - \lambda_0) \right)^2}, \quad (13)$$

Ideally, if the rate coefficient $|\mathbf{v}_Z| \cdot \sigma_{cx,eff}(|\mathbf{v}_Z|)$ in Eq. (11) was constant, the $\lambda-$dependence would only appear in the exponential term of Eq. (11). In this case, fitting a Gaussian to the measured spectrum allows to extract the accurate temperature and fluid velocity along the line of sight. However, as will be shown below, the rate coefficient increases with $|\mathbf{v}_Z|$ over most of the energy range of interest here. This means that faster impurity ions are more likely to emit a CX photon and the observed spectrum broadens. Ignoring this effect results in an overestimation of the impurity temperature. The special case with $\sigma_{cx,eff}(|\mathbf{v}_Z|) = const.$ and with no drifts, $\mathbf{u}_Z = 0$, can easily be treated analytically and fitting the obtained spectrum with a Gaussian would then result in an overestimation of the temperature by $\approx 50\%$. Besides a line broadening, our simplified treatment also shows that a rate coefficient increasing with $|\mathbf{v}_Z|$ leads to an overestimation of the line shift. To see this, let us assume a drifting Maxwellian for

the impurity ions with a drift velocity along the line of sight, away from the observer, such that the central wavelength shows a red shift. The particles moving away at a velocity higher than the drift velocity then have, on average, a larger $|\mathbf{v}_Z|$ and emit more CX photons than the other half of the particles which have a velocity along the line of sight smaller than the drift. This leads to an increase of the apparent line shift.

After these simplified cases, we now quantitatively treat more realistic situations to estimate errors in the measured values of T_Z and $u_{\parallel Z}$ caused by energy dependent rate coefficients. In particular, we relax the condition of static neutrals. Assuming Maxwellian velocity distributions for the impurity ions and donor particles and using effective emission cross-sections from ADAS[17], we solve Eqs. (9) and (10) with a Monte-Carlo scheme. We then fit the calculated spectra assuming a simple Gaussian shape to extract the apparent temperatures and flows and compare these with the true values. For the effective emission cross-sections, we consider Boron charge exchange with $D(n^D = 2)$ neutrals with a subsequent transition from $n = 7 \to 6$ of B^{4+}. These cross-sections include direct CX into the $n = 7$ level, as well as CX into higher n-levels with subsequent cascades into the $n = 7$ level, the branching ratio for the $n = 7 \to 6$ transition, l-mixing, and collisional excitations. In Fig. 7, we plot the rate coefficient $v_{col} \cdot \sigma_{cx,eff}(v_{col})$ as a function of $v_{col} = |\mathbf{v}_Z - \mathbf{v}_D|$, which now also depends on the velocity of the neutrals. The data in Fig. 7 is plotted up to v_{col} value that is $\sim 3 \cdot (v_{th,D} + v_{th,B})$, with the thermal velocities evaluated at $T_i = 1000$ eV. Cross-sections are plotted for an electron density n_e of 5×10^{18} m^{-3} (green), 5×10^{19} m^{-3} (blue), and 5×10^{20} m^{-3} (red). For each value of n_e, the ion temperature has been varied in the range $100 - 1000$ eV. Increasing ion temperature increases the cross-section, but this is a small effect. Fig. 7 shows that the rate coefficients increase approximately linearly with v_{col} over most of the energy range of interest here.

In a first step, we now evaluate errors in the apparent impurity temperature and flow for different values of T_Z, T_D, and $u_{\parallel Z}$, while setting $\mathbf{u}_D = 0$, $\mathbf{u}_{\perp Z} = 0$, and $n_e = 5 \times 10^{19}$ m^{-3}. Fig. 8 shows the relative error in T_Z for $u_{\parallel Z} = 0$ (solid blue) and $u_{\parallel Z} = 50$ km/s (dashed red), plotted as a function of T_D/T_Z. Curves of the same color correspond to different values of T_Z in the range 100 eV to 1000 eV. At zero flow, the different T_Z curves lie on top of each other. As expected from the analytic solution discussed above, the error in T_Z is approximately 50% for $T_D/T_Z = 0$. This error quickly reduces for finite T_D, reaching values $\lesssim 15\%$ for typical values of $0.3 < T_D/T_Z < 0.8$ (see Section II). Finite parallel flows reduce the error in T_Z, more importantly for lower values of T_Z.

Fig. 9 shows the plot analogous to Fig. 8 for the relative error in $u_{\parallel Z}$, revealing a similar behavior. While errors
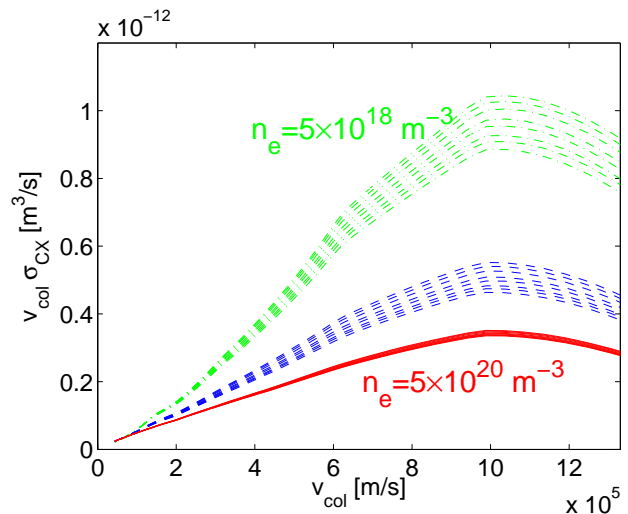

FIG. 7. Product of v_{col} and the effective emission cross-section for CX reactions between $D(n^D = 2)$ and B^{5+} with subsequent $n = 7 \to 6$ transition. Red solid, blue dashed, and green dash-dotted curves are obtained with data from ADAS for an electron density of 5×10^{20} m^{-3}, 5×10^{19} m^{-3}, and 5×10^{18} m^{-3}, respectively. Different curves of each color correspond to different values of T_i in the range 100 eV to 1000 eV.

also become smaller for larger parallel flows, especially for low impurity temperatures, this effect is weaker than for the temperature. Thus, both temperature and flows tend to be overestimated, in agreement with the qualitative discussion above.

In a next step, we have varied the electron density n_e. The results in Figs. 8 and 9 are found to be relatively weakly dependent on this quantity. Relative errors increase (decrease) by about 20% (10%) when n_e is decreased (increased) by an order of magnitude.

We have further looked at the effect of perpendicular flows, $\mathbf{u}_{\perp Z} \neq 0$. We find that the relative error in the apparent $u_{\parallel Z}$ decreases with increasing perpendicular flow in a similar way as it does with increasing parallel flow. Perpendicular flows also reduce the error in T_Z, but to a considerable smaller extent than parallel flows observed in Fig. 8.

Finally, the effect of a finite drift of the neutrals, $\mathbf{u}_D \neq 0$, can be estimated by applying Galilean transforms to the results above. Drifts of the neutrals can be expected in case of main ion flows, such that the main ions transfer not only their individual velocity, but also their macroscopic flow to the neutrals via CX reactions. This could cause large relative errors in $u_{\parallel Z}$ in situations where the drift of the impurities is low, while that of the neutrals is not. Let us assume for example that $u_{\parallel Z} = 0$ and that the drift of the neutrals (and that of the main ions) is $u_{\parallel D} = -50$ km/s. Transferring to a frame that moves at -50 km/s w.r.t. the lab frame, the neutrals and main ions have no drift and the impurities have $u'_{\parallel Z} = 50$ km/s. This is the situation solved in

Fig. 9. For $T_D/T_Z = 0.5$, the measured impurity flow is then overestimated by $\approx 10\%$ or about 5 km/s. Back in the lab frame, we would thus measure an apparent impurity flow of $u_{\parallel Z} \approx 5$ km/s, directed opposite to the movement of the neutrals.

Overall, we find that for experimentally relevant parameters, cross-section effects associated with GP-CXRS lead to an overestimation of impurity temperatures and flows of $\lesssim 15\%$. Currently, such errors are neglected in the analysis. Larger relative errors in the impurity flows could be expected in cases where the main ions have a large flow, particularly if it is opposite to that of the impurities, and if the main ions transfer that velocity to the neutrals.
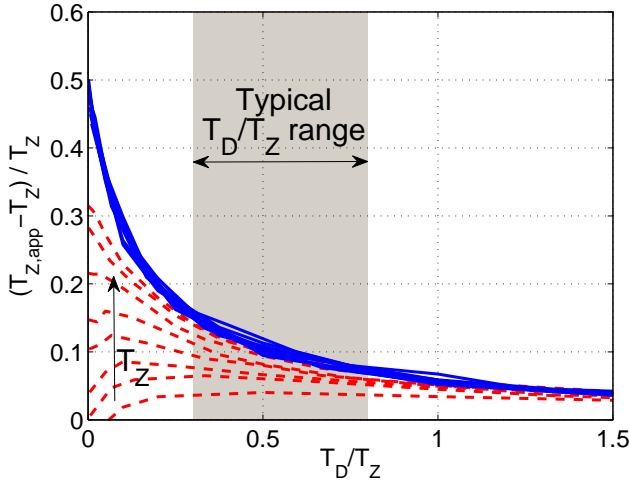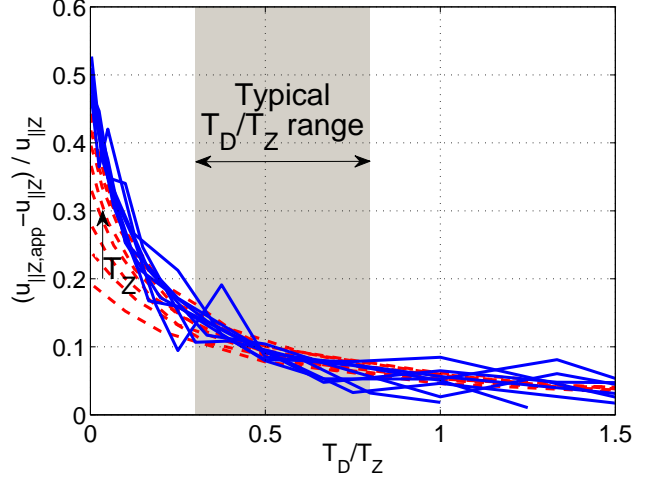

FIG. 9. The same as in Fig. 8 for relative errors in the apparent parallel flow. Here, blue curves correspond to a parallel flow of $u_{\parallel Z} = 5$ km/s.

FIG. 8. Relative errors in the apparent temperature as a function of T_D/T_Z obtained by solving Eqs. (9) and (10) with the cross-section data of Fig. 7 for $n_e = 5 \times 10^{19}$, $\mathbf{u}_{\perp Z} = 0$, and $u_{\parallel Z} = 0$ (blue), and $u_{\parallel Z} = 50$ km/s (dashed red). Different curves for a given color are obtained for different value of T_Z in the range 100 eV to 1000 eV. The arrow indicates increasing T_Z within dashed red curves. The shaded area highlights the experimentally relevant range of T_D/T_Z.

V.   ESTIMATES OF EXPECTED GP-CXRS SIGNAL

With the information on neutral penetration and effective CX rate coefficients given above, and an approximate impurity concentration in the plasma, estimates can be made to determine the GP-CXRS generated signal. Then, if the background emission (i.e. from Bremsstrahlung, CX with naturally occurring neutrals, and electron excitation of the hydrogen-like impurity, $A^{(Z-1)+}$) is known previously from measurement or modelling[32,33], the amount of injected gas needed for a particular signal/background ratio can be calculated.

The CXRS radiance is given by the usual equation:

$$I_{cx}(n' \to n'') = \frac{1}{4\pi} \sum_i \int_{LOS} dl \, q_{eff,i}(n', n'') n_{D,i} n_{A^{z+}}$$

(14)

where

I_{cx}	CXRS radiance of the atomic transition from upper level n' to lower level n'' $[photons/s/m^2/ster]$
$\sum_i$	Sum over the excited states of the neutral, i=1,2,3,...
$\int_{LOS} dl$	Integral over the optical line-of-sight (LOS)
$q_{eff,i}$	Effective CX rate coefficient $[photons \cdot m^3/s]$
$n_{D,i}$	Neutral density $[m^{-3}]$
$n_{A^{z+}}$	Impurity density $[m^{-3}]$

Simplifying (but accurate) assumptions can be made. First, if the optics are properly aligned to be tangent to flux surfaces at the point of emission, $q_{eff,i}$ and $n_{A^{z+}}$ can assumed to be constant over the LOS integral. Second, based on the discussion in Section III, the $D(n^D = 2)$ reaction will dominate. Using the expression for the $D(n^D = 2)$ density (Eq. (8) combined with Eq.(3), the equation for the $n^D = 1$ neutral density cloud) and plugging into Eq.(14), we arrive at the approximate signal:

$$I_{cx} \simeq \frac{1}{4\pi} q_{eff,2} \, n_{A^{z+}} \frac{PEC_{21}^{EXC}}{A_{21}} n_e n_{D0}(R) \sqrt{\pi} W(R)$$

(15)

A simple and quick procedure for calculating the neutral density profile, $n_{D0}(R)$, for use in estimating the GP-CXRS signal, is to use KN1D to simulate the $n_{D0}(R)$ profile, as the shape was found to match well with the OSM-EIRENE $n_{D0}(R)$ profile. To match the KN1D molecular pressure input (given in mTorr) to the diagnostically rel-

evant gas flow rate (which will match the absolute values of $n_{D0}(R)$), an effective area of the gas puff cloud must be used, since KN1D is a 1D code. This was found to be empirically $A_{eff} \simeq 2.7 \cdot 10^{-3}\,\mathrm{m}^2$. This corresponds to a radius of $r \simeq 2.9$ cm, which is characteristic of the gas puff extent. The conversion then from gas flow rate to KN1D input molecular pressure is[20]:

$$P_{KN1D} = \frac{u_{D_2}}{\frac{1}{4} \cdot 0.1333 \cdot \frac{1}{k_B T}\, \bar{v}\, A_{eff}} \qquad (16)$$

where

P_{KN1D}	KN1D input molecular pressure $[mTorr]$
u_{D_2}	Gas flow rate $[D_2\,particles/s]$
0.1333	Conversion factor $[m^{-3} \cdot J/mTorr]$
k_B	Boltzmann constant
T	Gas temperature (usually room temperature, $\sim 293[K]$)
$\bar{v}$	Molecular average velocity, $\sqrt{\frac{8k_B T}{\pi m_{D_2}}}$

An example of using Eq. (15) to estimate the GP-CXRS signal is shown in Fig. 10, compared to actual measured GP-CXRS signal. A constant impurity fraction $n_{B5+} = 0.01 \cdot n_e$ was assumed over the entire profile, which is a typical level for these types of plasmas past the pedestal top. On Alcator C-Mod, the LFS impurity density pedestal location can be significantly shifted inward with respect to the electron density pedestal location, due to the ionization energy of the impurity, and the possible presence of an inward pinch[34]. This constant impurity fraction case is then only expected to match beyond the impurity density pedestal top, which in this case is $R < 0.883$ cm. Of course, if the actual impurity density profile is known from other diagnostics, much better estimates can be obtained. After doing such an analysis, a user can adjust the input gas flow rate into KN1D to arrive at a desired signal level, I_{cx}, for the GP-CXRS system. This will give a simple, first estimate for the gas puff flow rate needed to generate a usable signal level. For more detailed estimates, full 3D modelling of the gas puff should be used.

VI. ALCATOR C-MOD GP-CXRS SYSTEM

The Alcator C-Mod GP-CXRS system was initially developed by B. Lipschultz and K. Marr in 2005[35] to measure HFS parallel flows[3]. The system has steadily expanded since then. At the time of this writing, the GP-CXRS system consists of two separate gas puff nozzles, located at the low-field side (LFS) midplane and the high-field side (HFS) midplane. Each gas puff location has its own separate set of in-vessel optical periscopes, one viewing poloidally (vertical at the midplane) and one viewing mainly toroidally (at the location of the gas puff, these views are parallel to the magnetic field). A summary table of these periscopes is given in Table I and Fig. 11.
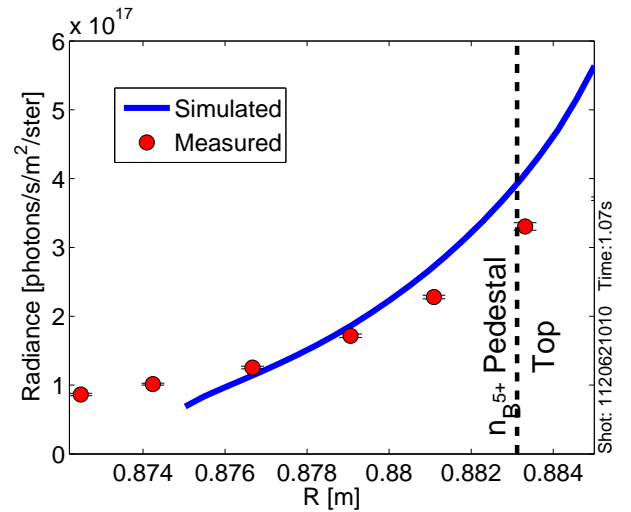

FIG. 10. Simulated CXRS radiance for views at the top of the pedestal, calculated from Eq. (15), assuming a constant $n_Z = 0.01 \cdot n_e$, using B^{5+} for the receiving ion. Agreement with measurement is within 20%
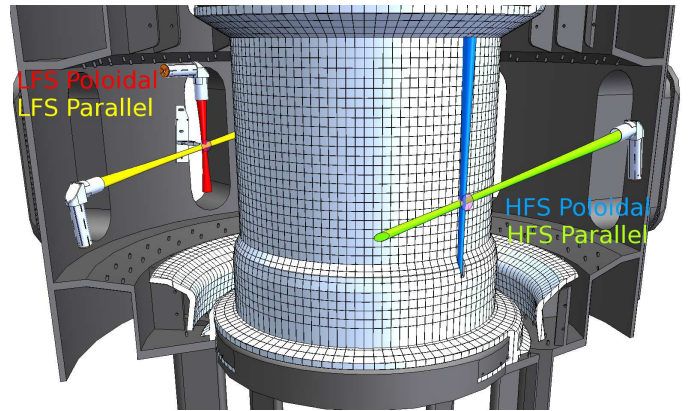

FIG. 11. Drawing of the in-vessel periscope setup for the Alcator C-Mod GP-CXRS system. Background periscopes are not shown.

Location	Angle of LOS w.r.t $\hat{\phi}$ [deg]	Spot Size [mm]	Typical r/a range	Typical # Views CXRS	Typical # Views D_α
Active (gas-puff viewing)					
LFS	-90	2.0	0.87 - 1.01	14	14
LFS	7	2.7	0.76 - 0.99	14	-
HFS	90	4.0	0.89 - 1.01	9	-
HFS	-10	4.0	0.89 - 1.01	9	9
Background/DNB					
LFS	-90	2.0	0.83 - 1.01	18	1
LFS	173	2.7	0.82 - 1.03	17	-
HFS	90	4.0	0.89 - 1.01	9	-
HFS	-10	4.0	0.89 - 1.01	9	-

TABLE I. Optical periscope information.

The gas puff nozzles are not nozzles at all, but simple gas capillary tubes, of 1mm inner-diameter and approximate length of 3 m. The outer-wall capillary is held in place by a dedicated structure made of Inconel, at a position of $R \simeq 0.92$ m (the limiter is at $R_{lim} = 0.905$ m). The inner-wall capillary is held in place by the wall-protection tiles, so is positioned at $R \simeq 0.44$ m. These capillary tubes are fed D_2 gas by the C-Mod Neutral INJection Apparatus (NINJA) system[36]. The NINJA system consists of a gas plenum of volume $1.26 \cdot 10^{-3}$ m^3, connected to several capillaries, with each individual capillary controlled by a pneumatic-actuated valve. There are two separate plenums which allow controlling the LFS and HFS gas capillaries with independent gas sources, though they can also be operated from a single plenum, as the volume is large enough to supply both capillaries. Typical input gas quantities for a gas puff used with the GP-CXRS system are ∼4 Torr·L, with a valve opening of 0.1 sec and a plenum pressure of 500 Torr. Because of trapped volumes and long tube lengths, the gas enters the vacuum chamber over a longer period of time[36]. Estimated peak flow rates are ∼$1.36 \cdot 10^{21}$ D^0atoms / s. An in-vessel image of the LFS gas puff is shown in Fig. 12, along with the normalized vertical line outs through the puff from various discharges, showing the gas puff shape is fairly constant for varying plasma parameters, in agreement with the OSM-EIRENE simulations (see Fig. 12).
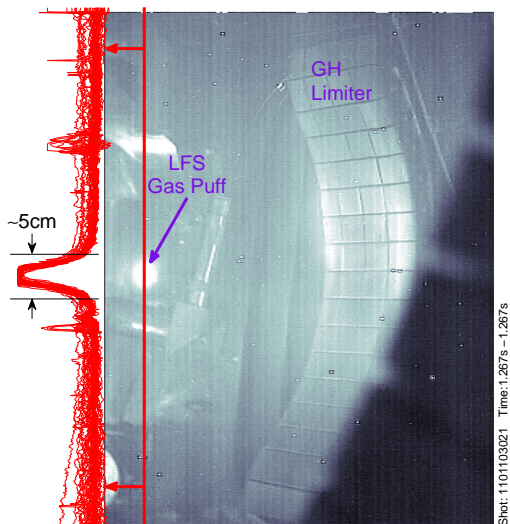

FIG. 12. In-vessel image of the LFS gas puff. Red lines to the left of the image are vertical line outs from 40+ shots (H-modes, I-modes, L-modes), showing the gas puff shape is similar for varying plasma parameters. The gas puff extent is about 5cm, in rough agreement with OSM-EIRENE simulations.

Optical periscopes are placed in-vessel, as the C-Mod port structure doesn't easily allow external views focused on the pedestal region. Optics focus the light onto $400\,\mu$m core diameter multimode fibers, which exit the vessel and are relayed to the spectrometer/CCD setup. Most periscopes are designed with two doublet achromat lenses, and a front surface mirror to prevent line-of-sight damage to the lenses. A snout measuring 9 cm extends from the mirror, and provides protection from gas films forming during the frequent wall-conditioning boronizations[37]. The exception to this general periscope design is the HFS poloidal periscope, which is embedded in the lower wall-protection tiles of the center stack. Due to the space constraints, this is a smaller periscope, with a single doublet achromat lens, and no mirror. The LFS poloidal and the HFS parallel periscopes have an extra row of fibers co-linear with the normal GP-CXRS fibers, but separated by a small distance (at the spot of best focus, 3mm). These extra fibers are used to measure neutral emission (usually $D_\alpha, \lambda = 656.10$ nm). The neutral emission measurements are used in the calculation of impurity density, as will be shown in Section VII. Additionally, optical periscopes are installed that don't intersect the gas puff, for use as effective background views, to remove passive light contribution to the GP-CXRS signal[32].

Two Kaiser spectrometers with a Volume Phase Holographic (VPH) grating are used to spectrally resolve the CXRS light[38]. These gratings have the benefit of large throughput, allowing 54 views (3 columns, 18 rows) to be imaged with a single spectrometer/CCD setup, but at the cost of fixed wavelength grating. Three of these views are sacrificed to image a neon lamp, for spectral calibration during an experiment. A high-cavity, 3 nm bandpass interference filter is used at the entrance of the spectrometer to allow 3 columns of fibers. Because of the fixed gratings, the C-Mod GP-CXRS system monitors exclusively the $BV(n' = 7 \rightarrow 6)(\lambda = 494.467)$ nm transition. The CCD used is a Princeton Instruments Photonmax, which has high quantum efficiency ($> 90\%$) and low readout noise (3 e-rms). A mechanical chopper is used to cover the CCD during frame transfer, since otherwise light from all other views in a column would add to each view, effectively smearing the spectra[39]. Integration times are typically 5 ms. Because the 54 views imaged on the CCD camera can have large differences in light levels (whether its a background, beam, or gas puff view), its desired to attenuate certain high light level views to prevent saturation, without having to reduce the signal levels globally, through the gain of the CCD, or the F-stop of the spectrometer input lens. For saturating views, short 1 m attenuator fibers with smaller core diameters (100, 200, or 300 μm) than the relay fiber are connected before the spectrometer fiber patch panel. These give an attenuation factor of $f \simeq D_{atten}^2/D_{relay}^2$, where D represents the fiber core diameter.

The neutral emission is not spectrally resolved, but rather its radiance is measured using Hamamatsu S8746-01 photodiodes. These photodiode packages have a built-

in pre-amp, with a specific gain setting $(1\,G\Omega)$, allowing for excellent low-noise light collection. Additional parallel feedback resistance can be added to the circuit to reduce the gain setting, and increase the response time $(t_{rise} = 0.35 \cdot 2\pi \cdot R_f C_f)$. Individual $H_\alpha(\lambda = 656.3\,\text{nm}, \Delta\lambda = 3\,\text{nm})$ interference filters were used on each photodiode to measure $D_\alpha(\lambda = 656.1\,\text{nm})$, with an optical collimator before the filter to prevent wavelength shifts of the filter central wavelength.

VII. ANALYSIS OF SPECTRA

Spectra obtained from the Alcator C-Mod GP-CXRS system is shown in Fig 13. As seen, the signal-to-background ratio is large, even at this spatial location, which is near the pedestal top. Deriving Doppler spectrometry quantities of radiance, velocity, and temperature from the GP-CXRS signal proceeds as in any other CXRS system: remove passive light contributions from the spectra, use a computational non-linear regression analysis to derive the moments of the spectra (taking care to remove instrument function and Zeeman effects[40]), then relate these moments with their physical quantities[25].
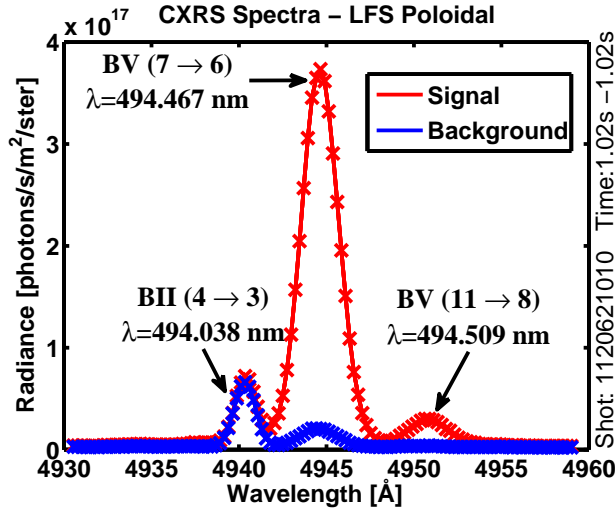
FIG. 13. Spectra from the GP-CXRS LFS poloidal periscope, showing signal enhancement over the background passive emission. Taken from a view in the pedestal top region.

Example profiles are shown in Fig 14 for an EDA H-mode[41]. Two differences that need to be addressed for the GP-CXRS system are the calculation of density from the radiance measurement, and spectral contamination by D_2 molecular lines.

A. Density

The density can be calculated using Eq. (14) with simulated n_D values, or measured neutral emission. The
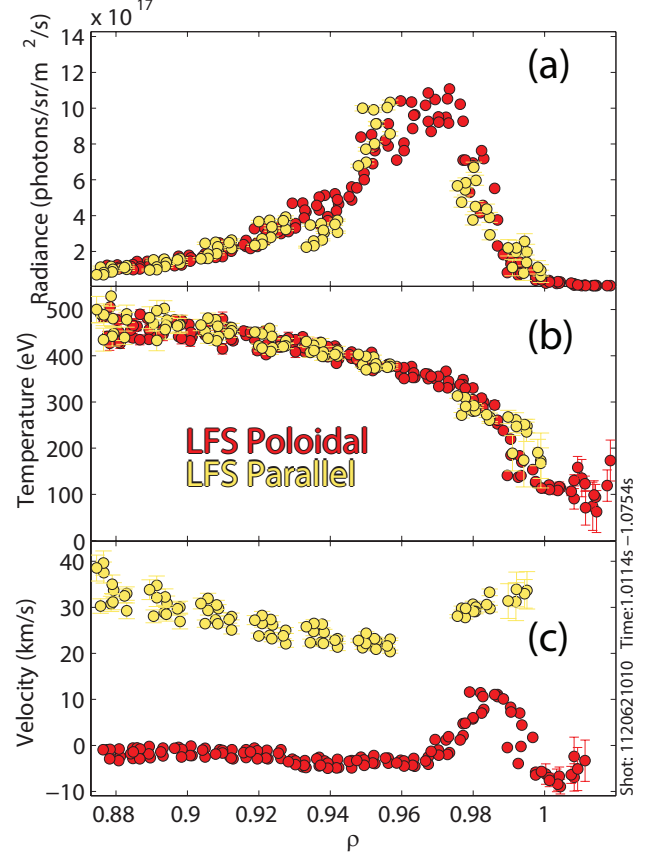
FIG. 14. Profiles from the GP-CXRS system. (a) radiance, (b) temperature, and (c) poloidal and parallel velocity. ρ here is a normalized major radius coordinate, roughly equal to r/a.

simulations are sensitive to input electron density and temperature profiles, including in the SOL. The SOL n_e and T_e profiles are not routinely measured on Alcator C-Mod in RF heated plasmas. Additionally, simulations don't resolve the time dependence of the gas puff. For these reasons, the measured neutral emission is generally preferred to the neutral simulations. In order to use the measurement, we must relate the excited neutral density, $n_D(n^D = 2)$ to the measured D_α radiance, I_{D_α}. The density $n_D(n^D = 2)$ can be related to the D_α emissivity, ε_{32}, with simple algebra and using the general equations relating emissivity to PEC coefficients[17]: $\varepsilon_{jk} = PEC_{jk}^{EXC} n_e n_D(n^D = 1)$ and spontaneous emission: $\varepsilon_{jk} = n_D(n^D = j)A_{jk}$. The expression for $n_D(n^D = 2)$ (Eq. 8) was found using these two general equations for the Lyman-α transition $(n^D = 2 \rightarrow 1)$. If we solve for $n_D(n^D = 1)$ in Eq. (8), and plug it into the equation for ε_{32}, we arrive at the desired equation relating excited state neutral density $n_D(n^D = 2)$ to the

D_α emissivity, ε_{32}:

$$n_D(n^D = 2) = \frac{1}{A_{21}} \frac{PEC_{21}^{EXC}}{PEC_{32}^{EXC}} \varepsilon_{32} \qquad (17)$$

where ε_{32} is the D_α emissivity in $[photons/s/m^3]$, A_{21} is the Einstein A coefficient $[s^{-1}]$ for the $n^D = 2 \to 1$ transition, and the PEC^{EXC} coefficients are photon emissivity coefficients from ADAS $[photons/s \cdot m^3]$. Turning again to Eq.(14), as long as q_{eff} and $n_{A^{z+}}$ are constant over the optical line-of-sight through the gas puff neutral cloud, they can be removed from the integral, leaving $\int_{LOS} dl\, n_{D,i}$. These assumptions were verified using 3D OSM-EIRENE simulations. Plugging in Eq. (17), and noting that the PEC coefficients depend on n_e and T_e, which likewise will be assumed constant over the intersection of the optical line-of-sight and the emission region, gives:

$$
\begin{aligned}
n_{A^{z+}} &= \frac{4\pi I_{cx}}{q_{eff,2}(n',n'') \frac{1}{A_{21}} \frac{PEC_{21}^{EXC}}{PEC_{32}^{EXC}} \int_{LOS} dl\, \varepsilon_{32}} \\[2mm]
&= \frac{A_{21}}{q_{eff,2}(n',n'')} \frac{PEC_{32}^{EXC}}{PEC_{21}^{EXC}} \frac{I_{cx}}{I_{D_\alpha}} \\[2mm]
&= f\left(n_e, T_e, T_i, T_D, Z_{eff}, n', n''\right) \frac{I_{cx}}{I_{D_\alpha}}
\end{aligned}
$$
$$(18)$$

where I_{D_α} is the D_α line-integrated emissivity (radiance) in $[photons/s/m^2/ster]$, and f is an atomic physics factor, with the dependencies on background plasma parameters shown explicitly. An example of the measured I_{D_α} signal is shown in 15, with the simulated I_{D_α} from OSM-EIRENE. The large discrepancy between measurement and simulation in the SOL ($\rho > 1$) could be due to overestimation of the molecular D_2 contribution to the D_α light, or incorrect inputs into the simulation (i.e. electron density and temperature in the SOL).

B. Contamination by Molecular Lines

The D_2 molecules of the puffed gas cloud are not immediately dissociated. Therefore, typically in the region of the last closed flux surface and further into the region of open magnetic field lines (the SOL), a whole zoo of molecular lines is observed. This is undesired as these lines overlap with the BV charge exchange line. An example is shown in Fig. 16, where the measured spectrum right before and after the gas puff is shown for the outermost view ($\rho \approx 1.04$) of the LFS poloidal periscope. For illustration, the position of tabulated molecular deuterium lines[42] is indicated with green vertical lines. The tabulated lines which are plotted are only the lines from Ref. 42 which have an assigned intensity in the I_2 column of that paper. These tabulated lines agree well with measured emission
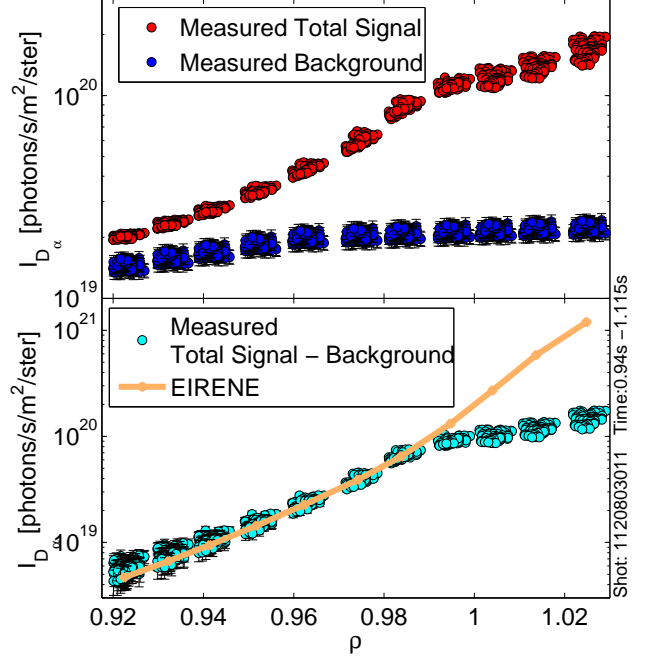

FIG. 15. (a) Measured D_α radiance, with the total (active + background) in red, and the background in blue. (b) Measured D_α radiance (I_{D_α}) in cyan, resulting from subtracting the background from the signal in (a). I_{D_α} simulated from OSM-EIRENE is shown in orange, showing good agreement with measured signal.

from a D_2 spectral lamp. Such a lamp can be used to determine whether D_2 lines exist which can interfere with a CX line of interest.
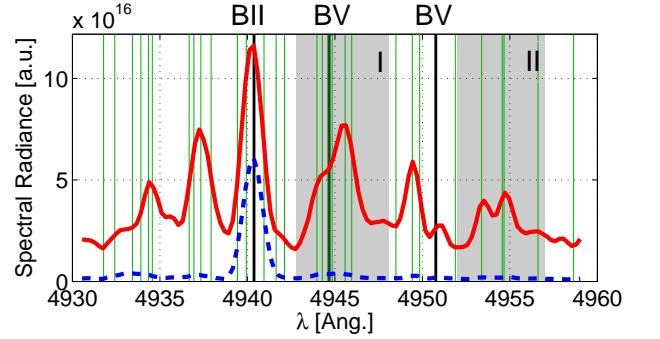

FIG. 16. Pre (blue dashed) and post (red solid) puff spectrum on the outermost view of the LFS poloidal periscope. The position of D_2 lines as tabulated in [42] are indicated by vertical green lines.

The parts of the spectra outside the wavelength region of the Boron lines can be used to detect the presence of D_2 lines. One can then exclude these spectra in the

analysis. Alternatively, one can try to estimate the D_2 contribution to the spectra in order to extract information on the B^{5+} population. In the following, we present a heuristic technique to achieve this. We then validate it using He puffs instead of D_2 puffs, which avoids the problem of contaminating lines in the spectra. We note here that the reason why He puffs are not used on all shots is that this produces a CX signal which is much lower and reaches less far into the plasma compared to D_2 puffs. Also, the CXRS system is not set up to measure the helium density necessary to calculate $n_{B^{5+}}$ (optical interference filters at a He emission wavelength would need to be purchased).

The technique presented here to estimate the D_2 contribution to the spectrum around the BV line is based on two assumptions. First, we assume that far in the SOL, the spectrum is entirely due to D_2 emission, i.e., we assume that the contribution of the BV line in the shaded region I in Fig. 16 is negligible with respect to the contribution from D_2. Second, we assume that all D_2 lines in the shaded areas I and II of Fig. 16 scale with the same factor as we move further into the plasma. To analyze a given spectrum, we then take the active spectrum in Fig. 16, scale it such that the amplitude of the lines in region II match those of the spectrum we want to analyze, and subtract the scaled spectrum over the spectral range of interest (region I). Region II is used as it is free from other spectroscopic lines that occasionally appear in other regions. The remaining spectrum is then fitted as usual, using a three gaussian, Blom-Jupin function[40], to extract intensity, central wavelength, and width of the BV line.

Fig. 17 shows an example spectrum and the contributions of D_2 and BV emission obtained with the described method. In order to see how sensitive the result is on the scale factor we apply to the D_2 spectrum, we vary it by $\pm 10\%$ and include the variation of the final fit parameters in the error bars of the deduced plasma parameters.
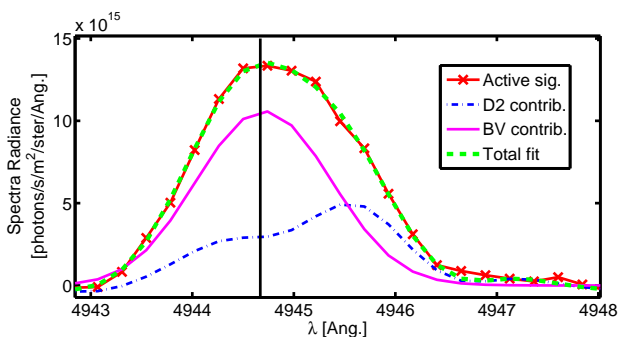

FIG. 17. Example of a fit to a spectrum where both the BV and D_2 lines contribute.

Fig. 18 shows profiles of brightness, ion temperature, and ion poloidal flow of B^{5+} for two similar shots, where D_2 and He was used for the gas puff, respectively. The profiles in green are obtained by analyzing data from the shot with the D_2 puff and ignoring the presence of molec-

ular lines. The blue data points are obtained for the same data, applying the D_2 subtraction technique described above. We can see that this fit results agree rather well with the data in red, obtained from the discharge with the He puff.

This analysis also clearly shows that a radially increasing ion temperature in the SOL, which one could infer from data with D_2 puffs, is not correct.
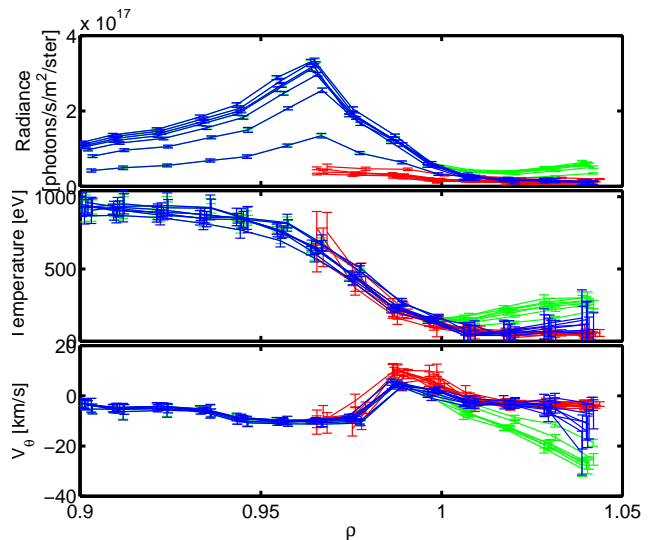

FIG. 18. A test of the D_2 subtraction method for an I-mode plasma (shots 1120828025/26). Green profiles are obtained from an analysis where the D_2 lines in the spectrum have been ignored. The blue profiles are obtained when the D_2 subtraction technique is applied. Red profiles are obtained from a similar shot where He was puffed instead of D_2.

VIII. HFS GP-CXRS SYSTEM AT ASDEX UPGRADE

At the ASDEX Upgrade (AUG) tokamak, two GP-CXRS diagnostics viewing the edge of the plasma at the HFS of the vessel are installed. The HFS systems utilize a deuterium (D_2) gas puff and collect the light that is emitted after the impurity undergoes a CX reaction with a thermal D particle. The HFS array consists of a toroidal[4] and a poloidal view (see figure 19) and each view is equipped with two $f/4$ optical heads. For the toroidal system, one optical head views the gas puff directly, while the other views the background plasma parallel to the active optical head (~ 10 cm above the active view) and thus, collects the corresponding background spectra. Both optical heads are installed at the LFS and view through the plasma edge at the outer midplane, intersect either the diagnostic gas puff at the HFS or the plasma edge at the inner wall for the background view, respectively. Then the views pass through the plasma edge at the other side (again LFS). Hence, the background optical head collects passive emission from three separate

regions along the LOS, while the active optical head collects additional emission from the HFS region when the gas puff is switched on. Similarly, the poloidal system has one optical head viewing the gas puff directly, while the second views the background plasma at the same poloidal location, but at a different toroidal location (sector 3, see figure 19) to avoid the active CX signal. These are both installed at the HFS and thus, collect light from the plasma edge at the inner wall. Due to the installation of two optical heads for each view, the background signals, i.e. the passive emission, can be subtracted from the active spectra. Each optical head is equipped with six LOS
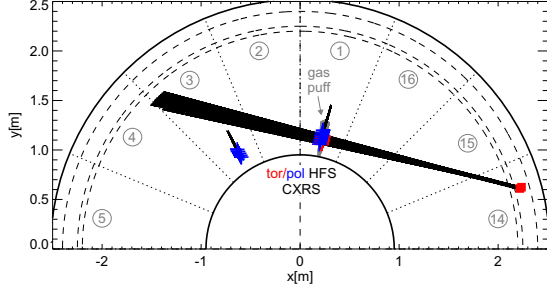

FIG. 19. Top-down view of AUG HFS GP-CXRS system

allowing a radial profile to be measured. In the focal plane the spot size of the LOS is 8.8 mm for the toroidal HFS system and 5 mm for the poloidal HFS diagnostic, while the channel spacing is 1.25 cm. The radial resolution can be increased by applying the radial plasma sweep technique[29] and moving the plasma position towards the inner wall. All optical heads are aligned such that they view the plasma as tangential to the flux surfaces as possible. The spectrometer system used is the same as that used for the toroidal view of the LFS beam-based CXRS system[29]. A major advantage of these spectrometers is their variable wavelength grating, allowing comparisons of the flows and temperatures of different impurities[4]. Example HFS profiles from the ASDEX Upgrade HFS GP-CXRS system are shown in figure 20.

IX. COMPARISON TO BEAM-BASED CXRS

In addition to the GP-CXRS system, Alcator C-Mod also has a traditional LFS CXRS system viewing a high-energy diagnostic neutral beam (DNB), that produces 50 keV hydrogen neutrals, with a total current of 7 A[43,44]. This provides a benchmark for comparing the resulting profiles derived from both systems. From Fig. 21 we can see the benefit of the GP-CXRS, especially in the pedestal region (for this shot, $0.97 < \rho < 1$) over that of the C-Mod beam based system. The active signal radiance in the pedestal is much higher for the GP-CXRS system, especially in the pedestal region, where the beam based system has little signal enhancement. This also shows that $\rho \sim 0.87$ is the furthest in point for which the GP-CXRS has comparable signal enhancement to the
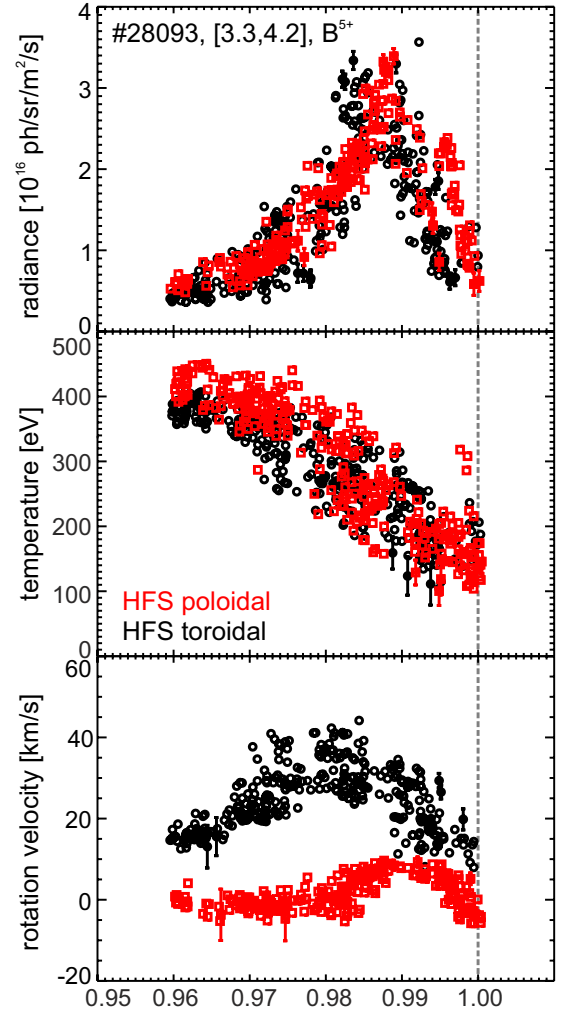

FIG. 20. Profiles from the AUG HFS GP-CXRS system, both poloidal and toroidal views

beam based system. Further in the signal will continue falling exponentially, limiting the GP-CXRS to measurements for $\rho > 0.85$.

For shots with the beam and the gas puff, the two CXRS systems produce similar n_Z, T_Z, and v_θ for the B^{5+} species, show in Fig. 22.

Notice the absence of $T_{B^{5+}}$ measurements from the beam based system starting near the top of the pedestal. The CXRS signal enhancement with the C-Mod DNB is often too low to resolve the pedestal temperature and velocities completely, a major detraction for the Alcator beam based CXRS system. The high signal to background ratio of GP-CXRS light may not be an advantage for LFS CXRS measurements on machines with heating beams, which can have comparable signal to background ratios. For these situations, the smaller width of the gas puff may still be beneficial, depending on machine size. Certainly on these machines GP-CXRS is still attractive for making CXRS measurements at locations not accessible by the heating beams, such as the HFS measurements
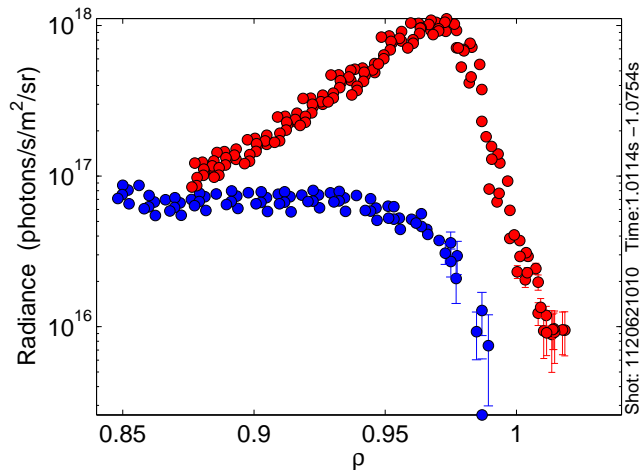
FIG. 21. Radiance from GP-CXRS (red) and DNB-CXRS (blue). The large signal, especially in the pedestal region, gives GP-CXRS great advantage over the beam based system.

on ASDEX Upgrade.

X. SUMMARY

The GP-CXRS technique developed in this paper allows measurements of ion parameters in the edge/pedestal region, with the benefits of large signal to background ratio, simple hardware, flexibility in measurement locations, and narrow emission region. The physics basis for the technique was reviewed, focusing on the characteristics of neutral transport and charge-exchange reactions at low energy. Using OSM-EIRENE simulations the gas puff neutral cloud was shown to have a canonical shape, but a large range in neutral density, varying with background density and temperature profiles. These neutral density profiles require a numerical kinetic neutral transport code to properly describe. For calculations of ion density, or expected CXRS signal, the thermal-thermal effective CX rate coefficient (q_{eff}) must be calculated, since the gas-puff neutrals have a thermal distribution. Cross-sectional effects were shown to be a small correction to the measured temperature and velocity ($< 15\%$). The hardware for the Alcator C-Mod GP-CXRS diagnostic and the ASDEX Upgrade GP-CXRS diagnostic was presented, along with measured spectra and profiles. Profiles measured with a LFS GP-CXRS system favor very well in comparison with the beam-based CXRS system.
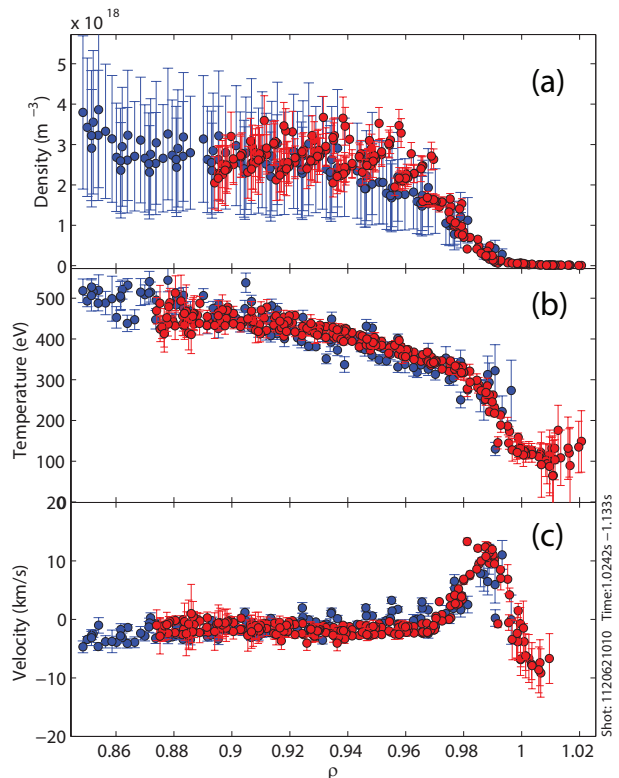
XI. ACKNOWLEDGMENTS

FIG. 22. Profiles of boron (B^{5+}) (a) density, (b) temperature, and (c) poloidal velocity from the GP-CXRS system (red) and the beam-based CXRS system (blue).

[1]R. J. Fonck, D. S. Darrow, and K. P. Jaehnig, Physical Review A, **29**, 3288 (1984).

[2]R. C. Isler, Plasma Physics and Controlled Fusion, **36**, 171 (1994), ISSN 0741-3335.

[3]K. D. Marr, B. Lipschultz, P. J. Catto, R. M. McDermott, M. L. Reinke, and A. N. Simakov, Plasma Physics and Controlled Fusion, **52**, 055010 (2010), ISSN 0741-3335.

[4]T. Pütterich, E. Viezzer, R. Dux, R. McDermott, and the ASDEX Upgrade Team, Nuclear Fusion, **52**, 083013 (2012), ISSN 0029-5515.

[5]R. Churchill, B. Lipschultz, C. Theiler, and J. Hughes, in *Bulletin of the American Physical Society*, Vol. 57 (2012).

[6]R. J. Groebner and T. H. Osborne, Physics of Plasmas, **5**, 1800 (1998), ISSN 1070664X.

[7]E. Doyle, W. Houlberg, Y. Kamada, V. Mukhovatov, T. Osborne, A. Polevoi, G. Bateman, J. Connor, J. Cordey, T. Fujita, X. Garbet, T. Hahm, L. Horton, A. Hubbard, F. Imbeaux, F. Jenko, J. Kinsey, Y. Kishimoto, J. Li, T. Luce, Y. Martin, M. Ossipenko, V. Parail, A. Peeters, T. Rhodes, J. Rice, C. Roach, V. Rozhansky, F. Ryter, G. Saibene, R. Sartori, A. Sips, J. Snipes, M. Sugihara, E. Synakowski, H. Takenaga, T. Takizuka, K. Thomsen, M. Wade, and H. Wilson, Nuclear Fusion, **47**, S18 (2007), ISSN 0029-5515.

[8]K. H. Burrell, Physics of Plasmas, **4**, 1499 (1997).

[9]R. Groebner, C. Chang, P. Diamond, J. Hughes, R. Maingi, P. Snyder, X. Xu, E. Belli, B. Bray, J. Candy, T. Deterly, N. Ferraro, J. Kinsey, A. Leonard, C. Liu, T. Osborne, D. Ponce, R. Prater, S. Smith, G. Staebler, R. Waltz, W. Stacey, M. Fenstermacher, I. Joseph, C. Lasnier, M. Umansky, E. Wang, X. Xu, D. Baver, D. DIppolito, J. Myra, D. Russell, R. Churchill, I. Cziegler, E. Davis, A. Hubbard, B. LaBombard, B. Lipschultz, Y. Ma, J. Rost, L. Sugiyama, J. Terry, J. Walk, A. White, D. Whyte, S. Wolfe, J. Canik, J. Lore, A. Sontag, D. Boyle, A. Diallo, S. Zweben, J. Watkins, A. Pankin, D. Fulton, Z. Lin, E. Doyle, T. Rhodes, L. Schmitz, L. Zeng, J. Boedo, D. Eldon, S. Parker, W. Wan, J. Elder, J. Callen, G. McKee, and Z. Yan, "Final report of the FES 2011 Joint Facilities and Theory Research Target," Technical report (Fusion Energy Sciences, 2011).

[10]H. Meyer, M. De Bock, N. Conway, S. Freethy, K. Gibson, J. Hiratsuka, A. Kirk, C. Michael, T. Morgan, R. Scannell, G. Naylor, S. Saarelma, A. Saveliev, V. Shevchenko, W. Suttrop, D. Temple, R. Vann, and the MAST and NBI teams, Nuclear Fusion, **51**, 113011 (2011).

[11]E. S. Marmar and Alcator C-Mod Group, Fusion Science and Technology, **51**, 261 (2007).

[12]B. Lipschultz, D. Whyte, and B. LaBombard, Plasma Physics and Controlled Fusion, **47**, 1559 (2005), ISSN 0741-3335.

[13]M. Tendler and D. Heifetz, Fusion Technology, **11**, 289 (1987).

[14]R. J. Goldston, *Introduction to Plasma Physics* (CRC Press, 1995).

[15]R. L. Boivin, J. A. Goetz, A. E. Hubbard, J. W. Hughes, I. H. Hutchinson, J. H. Irby, B. LaBombard, E. S. Marmar, D. Mossessian, C. S. Pitcher, J. L. Terry, B. A. Carreras, and L. W. Owen, Physics of Plasmas, **7**, 1919 (2000).

[16]K. H. Burrell, Physics of Plasmas, **10**, 2616 (2003).

[17]H. Summers, "ADAS User Manual," Tech. Rep. (University of Strathclyde, 2004).

[18]D. Stotler and C. Karney, Contrib. Plasma Phys., **34**, 392 (1994).

[19]D. Reiter, M. Baelmans, and P. Börner, Fusion Science and Technology, **47**, 172 (2005).

[20]B. LaBombard, "KN1D: A 1-D Space, 2-D Velocity, Kinetic Transport Algorithm for Atomic and Molecular Hydrogen in an Ionizing Plasma," Technical report (MIT Plasma Science and Fusion Center, 2000).

[21]T. Fülöp, P. J. Catto, and P. Helander, Physics of Plasmas, **8**, 5214 (2001).

[22]W. Wan, S. E. Parker, Y. Chen, G. Y. Park, C. S. Chang, and D. Stotler, Physics of Plasmas, **18**, 056116 (2011).

[23]R. E. Olson, Physical Review A, **24**, 1726 (1981).

[24]R. Janev and H. Winter, Physics Reports, **117**, 265 (1985), ISSN 03701573.

[25]I. Hutchinson, *Principles of Plasma Diagnostics* (Cambridge University press, 2002).

[26]F. Guzmán, L. F. Errea, C. Illescas, L. Méndez, and B. Pons, Journal of Physics B: Atomic, Molecular and Optical Physics, **43**, 144007 (2010), ISSN 0953-4075.

[27]J. P. Freidberg, *Plasma Physics And Fusion Energy* (Cambridge University press, 2007).

[28]J. Ghosh, H. R. Griem, R. C. Elton, J. L. Terry, E. Marmar, B. Lipschultz, B. LaBombard, J. E. Rice, and J. L. Weaver, Physics of Plasmas, **11**, 1033 (2004).

[29]E. Viezzer, T. Pütterich, R. Dux, R. M. McDermott, and the ASDEX Upgrade Team, Review of Scientific Instruments, **83**, 103501 (2012).

[30]K. H. Burrell and J. M. Muñoz Burgos, Physics of Plasmas, **19**, 072507 (2012).

[31]B. J. Ding, Y. Sakamoto, and Y. Miura, Plasma Physics and Controlled Fusion, **47**, 789 (2005), ISSN 0741-3335.

[32]M. Tunklev, P. Breger, K. Günther, M. von Hellermann, R. König, M. O'Mullane, and K.-D. Zastrow, Plasma Physics and Controlled Fusion, **41**, 985 (1999), ISSN 0741-3335.

[33]E. Viezzer, T. Pütterich, R. Dux, and A. Kallenbach, Plasma Physics and Controlled Fusion, **53**, 035002 (2011), ISSN 0741-3335.

[34]T. S. Pedersen, R. Granetz, A. Hubbard, I. Hutchinson, E. Marmar, J. Rice, and J. Terry, Nuclear Fusion, **40**, 1795 (2000), ISSN 0029-5515.

[35]K. Marr, B. Lipschultz, B. LaBombard, and J. Terry, Journal of Nuclear Materials, **337-339**, 286 (2005), ISSN 00223115.

[36]D. Jablonski, *Local Gas Injection as a Scrape-off Layer Diagnostic on the Alcator C-Mod Tokamak*, Phd, Massachusetts Institute of Technology (1996).

[37]B. Lipschultz, Y. Lin, E. Marmar, D. Whyte, S. Wukitch, I. Hutchinson, J. Irby, B. LaBombard, M. Reinke, J. Terry, and G. Wright, Journal of Nuclear Materials, **363-365**, 1110 (2007), ISSN 00223115.

[38]R. E. Bell, Review of Scientific Instruments, **75**, 4158 (2004).

[39]R. E. Bell, L. E. Dudek, B. Grek, D. W. Johnson, and R. W. Palladino, Review of Scientific Instruments, **70**, 821 (1999).

[40]A. Blom and C. Jupen, Plasma Physics and Controlled Fusion, **44**, 1229 (2002), ISSN 07413335.

[41]M. Greenwald, R. Boivin, P. Bonoli, R. Budny, C. Fiore, J. Goetz, R. Granetz, A. Hubbard, I. Hutchinson, J. Irby, B. LaBombard, Y. Lin, B. Lipschultz, E. Marmar, A. Mazurenko, D. Mossessian, T. S. Pedersen, C. S. Pitcher, M. Porkolab, J. Rice, W. Rowan, J. Snipes, G. Schilling, Y. Takase, J. Terry, S. Wolfe, J. Weaver, B. Welch, and S. Wukitch, Physics of Plasmas, **6**, 1943 (1999).

[42]R. S. Freund, J. A. Schiavone, and H. M. Crosswhite, Journal of Physical and Chemical Reference Data, **14**, 235 (1985).

[43]R. M. McDermott, *Edge Radial Electric Field Studies Via Charge Exchange Recombination Spectroscopy on the Alcator C-Mod Tokamak*, Phd, Massachusetts Institute of Technology (2009).

[44]R. M. McDermott, B. Lipschultz, J. W. Hughes, P. J. Catto, A. E. Hubbard, I. H. Hutchinson, R. S. Granetz, M. Greenwald, B. LaBombard, K. Marr, M. L. Reinke, J. E. Rice, D. Whyte, and the Alcator C-Mod Team, Physics of Plasmas, **16**, 056103 (2009), ISSN 1070664X.